Photothermal catalytic activity of combustion synthesized $LaCo_xFe_{1-x}O_3$ ($0 \leq x \leq 1$) perovskite for CO_2 reduction with H_2O to CH_4 and CH_3OH†

Lijuan Xu,[a] Minh Ngoc Ha,[c] Qiangsheng Guo,[b] Lichao Wang,[a] Yanan Ren,[a] Na Sha*[b] and Zhe Zhao*[ad]

A range of $LaCo_xFe_{1-x}O_3$ perovskites with different Co-doping at the B-site were successfully synthesized *via* a sol−gel combustion route. Phase pure samples were obtained by calcination at 700 °C for 2 h. The morphology, crystal structure, surface area, band structures, oxygen vacancies and catalytic properties of each analog were characterized in detail. The band structures and oxygen vacancies of the catalysts were changed by adjusting the dopant concentration. The catalytic performance of the $LaCo_xFe_{1-x}O_3$ materials was characterized using water as a hydrogen source in the production of CH_4 and CH_3OH from CO_2. Under photothermal conditions, 350 °C with a visible light source equipped with 420 nm cut filter, it was found that x value will influence the total yield and the solar to CH_4 and CH_3OH energy conversion efficiency significantly. For $x = 0.6$ compound, the production of CH_4 and CH_3OH evolution can reach 437.28 and 13.75 µmol g^{-1} in 6 h, which were 3.2 and 4.0 times that of $LaFeO_3$ under the same condition. The overall solar-to-methane efficiency and solar-to-methanol efficiency for $LaCo_{0.6}Fe_{0.4}O_3$ were 0.603%, 0.019% and for $LaFeO_3$ were 0.191%, 0.005% in the photothermal mode, respectively. The results show that the band gap energy is correlated with the photothermal activity and the $LaCo_{0.6}Fe_{0.4}O_3$ has the position of the CB and VB more suitable for CO_2 reduction. The CB and VB value of $LaCo_{0.6}Fe_{0.4}O_3$ were −0.258 and +1.422 V and CO_2 (−0.24 V for CB) can be reduced to methane under the conditions.

Introduction

Global industrialization leading to rising energy demand has resulted in a substantial increase in CO_2 emissions worldwide.[1] It is now broadly accepted that this increase is having a significant impact on the environment.[2,3] Finding a solution to this problem has become a global research focus with many investigators using conventional physical capture and storage techniques to control produced CO_2.[4,5] However, there are numerous drawbacks to this approach, such as low capture efficiency, high process cost, high energy consumption and potential environmental hazards.[6] Compared with this traditional physical method, chemical utilization is more economically favorable and to convert CO_2 into hydrocarbon fuels was

quite attractive.[7] A more environmentally robust solution is to convert CO_2 into raw chemical materials using solar energy.[8,9] This approach has the dual advantages of addressing the CO_2 emissions from factories, cars and other sources while providing by-products that are raw materials for future use as fuels.[10]

Photocatalysis is an emerging field of catalysis that has developed over the last 20 years. Given the environmental impact of current energy consumption practices, photocatalysis has the potential to provide a promising green and efficient alternative. A number of different semiconductor materials are being used as photocatalysts.[11–14] The electrochemical splitting of water using TiO_2 as a catalyst, published by Fujishima and Honda in 1972, is regarded as the beginning of photocatalysis.[15] TiO_2 has since been studied extensively owing to its efficiency, stability, and low cost. But its wide band gap requires the use of ultra-violet energy to initiate the reactions, resulting in its photocatalysis in the existence of some limitations. Photocatalytic reduction of CO_2 is a viable method for converting CO_2 into chemical raw materials (carbon compounds such as inorganic carbonates, methane and methanol) and has considerable significance in carbon recycling.[16,17] Since Hiroshi reported the photocatalytic reduction of CO_2 into organic compounds over semiconductor particles suspended in water,[18] a new

[a]School of Materials Science and Engineering, Shanghai Institute of Technology, Shanghai 201418, China. E-mail: zhezhao@kth.se

[b]School of Chemical and Environmental Engineering, Shanghai Institute of Technology, Shanghai 201418, China. E-mail: shana8033@163.com

[c]Faculty of Chemistry, Hanoi University of Science, Vietnam National University, Hanoi 10000, Vietnam

[d]Department of Materials Science and Engineering, KTH Royal Institute of Technology, SE-100 44 Stockholm, Sweden

method combining photo, thermal, electrical and chemical processes on the basis of photocatalysis has been developed by researchers. This approach improved the conversion rate for the reduction of CO_2 to CO, C and O_2 and H_2O to H_2 and O_2, compared with conversion rates for photo or thermal catalysis alone.[19,20]

Perovskites, which have the general formula ABO_3, are materials of potential owing to their stability, magnetism, crystal structure, electrical conductivity and piezoelectric properties. These advantages give rise to applications in magnetoresistance devices,[21–23] as solid electrolytes,[24] as transducers[25–28] and in catalysis.[29–32] Many perovskite materials have good response in the ultraviolet region. Among them, transition metal based $LaFeO_3$ is a visible light active material, which is suitable for the use of renewable solar energy as a light source to excite electrons for the CO_2 reduction. $LaFeO_3$ has shown great promising in terms of catalytic activity in the photocatalytic decomposition of water and the degradation of organic pollutants.[34–38] The efficiency of a material in harnessing solar energy is related to its band gap, which determines the range of the incident photon band that can be absorbed and can further affects the photocatalytic activity.[39] For the typical ABO_3 perovskite, both A- and B-site can be substituted to modify the local electronic structure, band gap and oxygen vacancy concentration in order to realize versatile properties.[33,40] In some case, the band gap of $LaFeO_3$ can even be modified through variation of the calcination temperature.[41] In this study, we try to modify the band gap and the relative position of the valence band and the conduction band through partial substitution of Fe by Co at the B-site in $LaFeO_3$ to investigate photothermal catalytic efficiency of materials.

In a typical experiment, the catalysts in accordance with formula $LaCo_xFe_{1-x}O_3$ perovskites were synthesized via a sol–gel combustion route and were calcined in air for 2 h at different temperatures between 500 and 900 °C. Then the synthesized samples were characterized using a range of scientific researching instruments (S1†). The whole experiment have been carried out in a catalytic reactor as show in Fig. 1. The reaction was in a gas tight circulation system, the volume of the reaction system was about 130 mL. The evaluation of catalytic activity was performed at 350 °C and used a 300 W Xe lamp with a UV-light filter ($\lambda > 420$ nm). Taking a sample every hour and qualitatively analyzed by GS-Tek (Echromtek A90) and quantitatively analyzed by gas chromatograph equipped with a flame ionization detector (S1†). Finally, the catalytic performance of $LaCo_xFe_{1-x}O_3$ ($x = 0$, 0.2, 0.4, 0.6, 0.8, 1) are reported, with the photothermal reduction of CO_2 with H_2O vapor to CH_4 used to probe catalytic activity. The influence of Co content on the perovskite band gap, the CB and VB positions, oxygen vacancies and resulting photothermal activity for the CO_2 reduction are revealed in detail.

Results and discussion

Impurity phases within a crystal structure can have a substantial effect on the mechanical and electrical properties of a material. The XRD patterns of $LaCo_{0.4}Fe_{0.6}O_3$ nanoparticles prepared at different calcination temperatures are shown in Fig. 2a. Through comparison with the characteristic peaks of the perovskite $LaFeO_3$ (Fig. 2b), we conclude that the Co-doped samples have perovskite structures and contain no noticeable impurities.[41] The diffraction peaks display an increase in intensity and narrowing in width with increasing calcination temperature, indicating that the perovskite crystallinity is affected by temperature. For the samples calcined at 500 and 600 °C, the $LaCo_{0.4}Fe_{0.6}O_3$ nanoparticles, which belong to the $Pm\bar{3}m$ space group, have a cubic perovskite structure. The a values of the perovskites calcined at 500 and 600 °C were 3.9065 and 3.8912, respectively.

The diffraction peaks for samples calcined at 700, 800 and 900 °C suggest that these samples exhibit orthorhombic crystal systems with an ABO_3 type perovskite structure (JCPDS card no. 01-081-2301), which belong to the $Pnma$ space group. The crystallite sizes determined by the Scherrer equation are 73.85, 34.73, 24.67, 31.59 and 59.54 nm for the samples calcined at 500, 600, 700, 800 and 900 °C, respectively. The small crystallite sizes favored the surface reaction kinetic and electrical transport properties of the catalysts. Thus calcination temperature of 700 °C was chosen for all samples in the subsequent
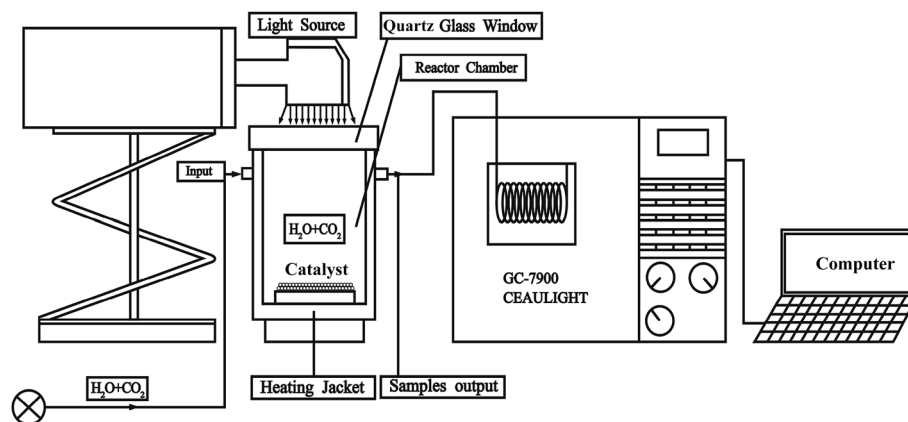

Fig. 1 Photothermal catalytic reactor for CO_2 reduction study.

experiments in order to promise both small crystallite size and reasonably good crystallinity.

The XRD patterns of $LaCo_xFe_{1-x}O_3$ (x = 0, 0.2, 0.4, 0.6, 0.8 and 1) nanoparticles prepared using the sol–gel combustion method with calcination at 700 °C for 2 h, are shown in Fig. 2b. Analysis of the characteristic peaks revealed no significant impurity phases. As the partial substitution of Fe by Co increases, we see that the peak intensity decreases and some of the peaks become split, the diffraction peaks shift regularly to the right, because of the greater strength of Fe–O bonding compared with Co–O bonding.[23] Additionally it was observed that the perovskite structure is orthorhombic when the Co-doping level is 0, 0.2 or 0.4, however the structures are trigonal for crystals with Co-doping from 0.6 to 1. This suggests that Co-doping changes the lattice structure and x = 0.4–0.6 might be the region that two phases co-existed simultaneously, even we can't see that clearly from the XRD patterns. In addition, the crystallite size determined by the Scherrer equation can be also affected by the Co concentration in $LaCo_xFe_{1-x}O_3$ as shown in Table 1.

The specific surface areas and pore sizes of the $LaCo_xFe_{1-x}O_3$ catalysts with the different substitutions (x) by using nitrogen adsorption–desorption isotherms at 77 K on a Micrometrics ASAP 2020 HD88 systems, are listed in Table 2. Except for the pure $LaCoO_3$, the specific surface area of the samples changed within a limited range and thus the catalytic performance for samples of x = 0, 0.2, 0.4, 0.6 and 0.8 can be comparable if we believe that surface reaction dominated the most catalysis process.

Table 2 The surface properties of the catalysts were examined by BET surface area

Ratio of Co doping (x)	Surface area (BET) m^2 g^{-1}	Pore size (nm)
0.0	9.2853	28.29821
0.2	7.3525	44.57917
0.4	8.4393	26.57818
0.6	9.7343	21.50945
0.8	5.1724	19.76648
1.0	2.7064	73.00958

The SEM images of $LaCo_xFe_{1-x}O_3$ nanoparticles calcined at 700 °C are shown in Fig. 3a–f. As would be expected as a result of sol–gel combustion synthesis, it can be seen that the samples are porous materials. Comparing these micrographs with that of a pure $LaFeO_3$ sample, reveals subtle differences in particle morphogenesis. Samples with a Co-doping of 0.2, 0.4 and 0.6 (Fig. 3b–d) exhibited increasingly rounded particles as the amount of cobalt increased, and showed greater porosity. When Co-doping is raised to 0.8 and 1, aggregation growth among the particles is clearly observed, which is expected to lead to a reduction in catalytic activity. The SEM images also reveal that the pores of the samples with Co-doping of 0.8 and 1 are isolated. This contrasts with the samples with lower doping ratios where the channels or pores are interconnected. Furthermore, their particle size is 100 nm. Consequently, we propose that the Co to Fe molar ratios of 0.2, 0.4 and 0.6 provide the most suitable morphology for good catalytic activity. Ratios above 0.6
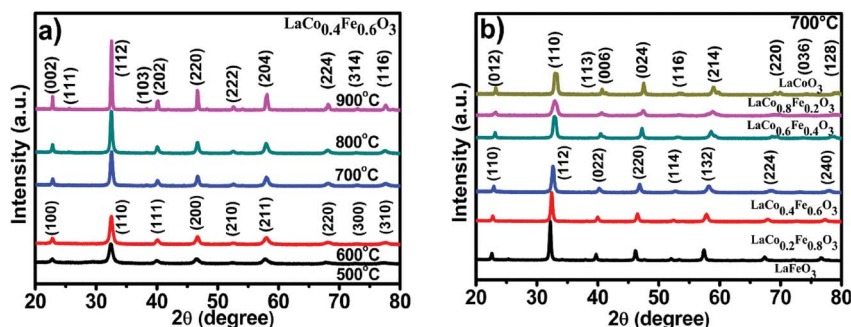

Fig. 2 (a) XRD of $LaCo_{0.4}Fe_{0.6}O_3$ nanoparticles at different temperature, (b) $LaCo_xFe_{1-x}O_3$ photocatalyst at different Co-doping at 700 °C for 2 h.

Table 1 The XRD analysis results

Samples (x)	Crystal system	2-Theta (degree)	d(112) (nm)	Unit cell a, b, c (nm)	Crystallite size (nm)
0.0	Orthorhombic	32.1818	0.277923	5.5601, 5.5651, 7.8562	32.7808
0.2		32.3892	0.276191	5.5171, 5.5201, 7.8184	26.8103
0.4		32.5459	0.274897	5.5022, 5.5410, 7.7713	24.6748

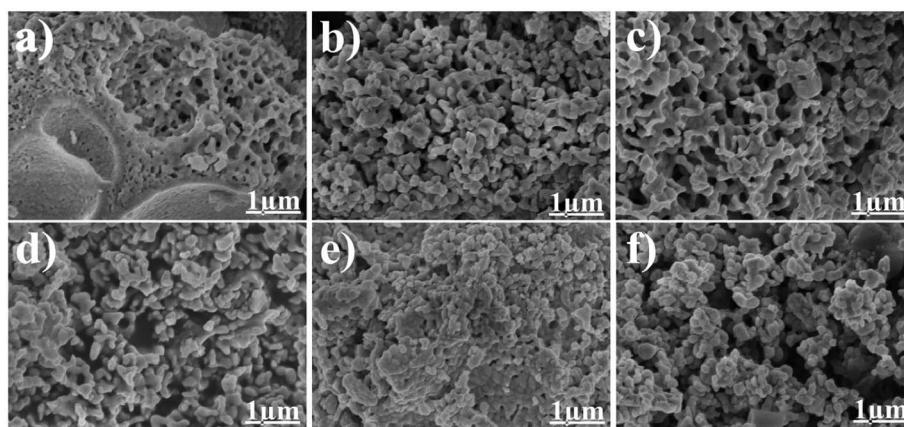| Samples (x)	Crystal system	2-Theta (degree)	d(110) (nm)	Unit cell a = b, c (nm)	Crystallite size (nm)
0.6	Trigonal	32.7522	0.273212	5.4610, 13.116	20.6059
0.8		32.8838	0.272149	5.4378, 13.164	56.8321
1.0		32.8977	0.272037	5.4441, 13.112	48.7331

Fig. 3   SEM images of LaCo$_x$Fe$_{1-x}$O$_3$ nanoparticle in different Co rate at (a) 0, (b) 0.2, (c) 0.4, (d) 0.6, (e) 0.8, (f) 1 at 700 °C for 2 h.

promote crystallite growth, leading to larger particle size and lower BET surface area.

More detailed information on LaCo$_{0.6}$Fe$_{0.4}$O$_3$ nanoparticle morphology is presented in the TEM images in Fig. 4. The image in Fig. 4a shows that small nanoparticles with an average size of 50–100 nm form larger agglomerations composed of interconnected nanocrystal skeletons. These observations support the SEM findings. In addition, the TEM image in Fig. 4b shows clear lattice spacing (d values) for the LaCo$_{0.6}$Fe$_{0.4}$O$_3$ nanoparticles. The interplanar (110) spacing of the LaCo$_{0.6}$Fe$_{0.4}$O$_3$ nanoparticle was determined to be 0.27 nm by TEM. This corresponds with the (110) lattice spacing of the trigonal phase of the perovskite crystal structure from the XRD analysis, and is the same as XRD Rietveld structure refinement results for
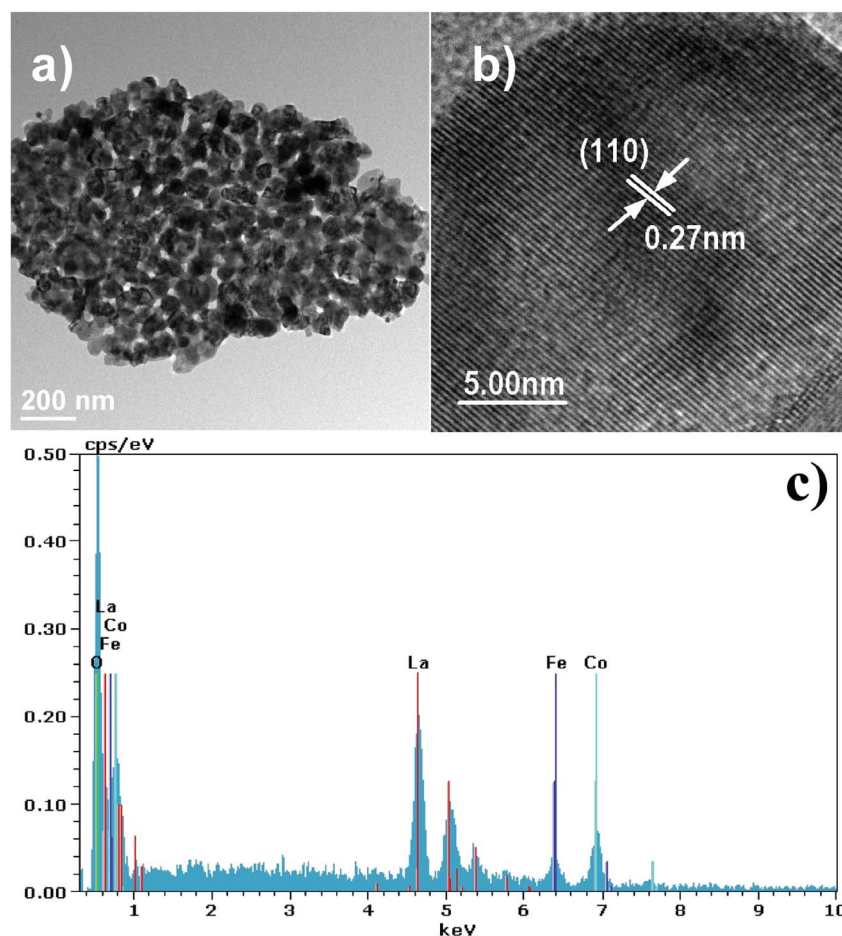

Fig. 4   (a and b) TEM images and (c) EDS images of LaCo$_{0.6}$Fe$_{0.4}$O$_{3-\delta}$ prepared at 700 °C for 2 h.

$LaSrCoFeO_{6-\delta}$. A Bruker-AXS 133 eV XFlash 4010 Detector associated with the SEM was used to measure the elemental composition of the $LaCo_{0.6}Fe_{0.4}O_3$ as well as the nature of the distribution. From the EDS spectrum and the elemental mapping images in Fig. 4c, it can be seen that La, Fe, Co and O dominate the composition of $LaCo_{0.6}Fe_{0.4}O_3$. These data support the uniform distribution of La, Fe, Co and O within the $LaCo_{0.6}Fe_{0.4}O_3$ catalyst.

The chemical state and surface species of the $LaCo_xFe_{1-x}O_3$ catalysts were established by XPS analysis as shown in Fig. 5. The survey spectra (Fig. 5d) show peaks that are ascribed to La, Fe, Co, O and C. No peaks corresponding to other elements were observed. Table 3 reports the binding energies of the $LaCo_xFe_{1-x}O_3$ perovskites, which provide evidence of the coexistence of at least two oxidation states for both the Co and Fe regions. Peak deconvolutions are shown in Fig. 5a and b. These observations agree with the literature.[20,42,43] The oxidation states for both Fe and Co at the B-site were 2^+ and 3^+. The cobalt region shows the typical Co 2p pattern with Co $2p_{3/2}$ and Co $2p_{1/2}$ as shown in Fig. 5a, and also includes the respective shake-up satellite peaks. The Co $2p_{3/2}$ binding energies attributed to Co^{2+} and Co^{3+} were observed at 780 and 782 eV respectively. The Co $2p_{1/2}$ binding energy resolved into Co^{2+} and Co^{3+} contributions centered at 794 and 796 eV, respectively.[43,44] The Fe 2p peak fitting of the $LaCo_xFe_{1-x}O_3$ catalyst was performed according to the constraints of the Fe^{2+} and Fe^{3+} components and the respective shake-up satellites indicated by Liu.[45] The high binding energy of the second component of iron in the

table is attributed to Fe^{3+}.[42,46] The presence of doublets characteristic of Co 2p (Co^{3+}) and Fe 2p (Fe^{3+}) was observed for the samples, together with two bands corresponding to O 1s. These bands can be attributed to the lattice, surface and absorbed oxygen.[47] The absorbed oxygen has been omitted from Table 4 with only the lattice and surface components used to calculate the relative amounts of the two types of oxygen. Interestingly, it has been reported that the surface oxygen component develops with the increase of oxygen vacancies,[48] and the lattice component decreases with decreasing iron content, indicating an increase in the oxygen vacancies,[44] which can lead to asymmetry of the main peak. It has also been reported that high-resolution O 1s XPS spectra indicate that the peak area of surface oxygen peaks obviously decreased with increasing catalytic reaction times.[33] Besides, the O 1s signal of the $LaCo_{0.6}Fe_{0.4}O_3$ perovskite was shows as well. The photothermal catalytic activities for CO_2 conversion with H_2O vapor to CH_4 over $LaCo_{0.6}Fe_{0.4}O_3$ catalysts showed that the catalytic activity depends on Co^{3+}/Co^{2+}, Fe^{3+}/Fe^{2+} (detail in Table 3).

The diffuse reflectance spectra of $LaCo_xFe_{1-x}O_3$ perovskites prepared at different Co-doping molar ratios were measured and are shown in Fig. 6a. From the optical absorption spectra, we can see that the samples had a complete absorption edge. The results indicate that $LaCo_xFe_{1-x}O_3$ nanoparticles are active in the visible light region, therefore, the properties of the samples can be tested using visible light driven methods.

To estimate the optical band gap (E_g) of the prepared samples, we used acquired data in the following equation:
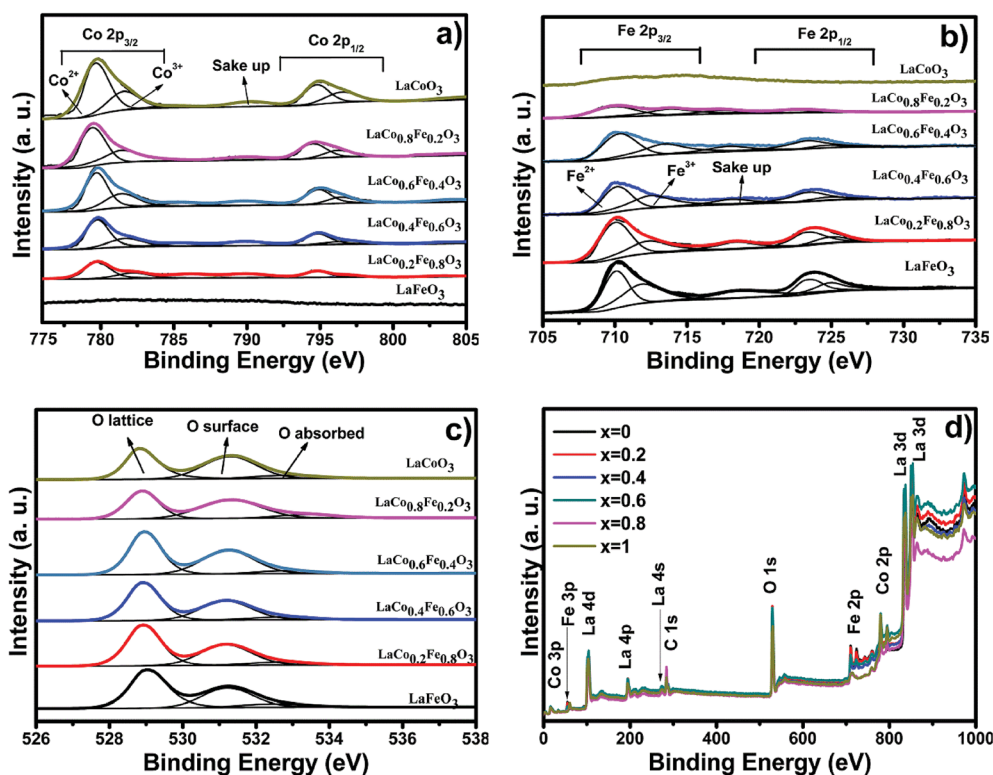

Fig. 5 The XPS spectra of (a) Co 2p, (b) Fe 2p, (c) O 1s and (d) survey spectra of $LaCo_xFe_{1-x}O_3$ (0, 0.2, 0.4, 0.6, 0.8, 1) catalyst prepared at 700 °C for 2 h.

Table 3   XPS binding energies relative to the perovskites $LaCo_xFe_{1-x}O_3$

Catalyst (x)	Co 2p (eV)		Fe 2p (eV)	
	Co 2p$_{3/2}$(%)	Co 2p$_{1/2}$(%)	Fe 2p$_{3/2}$(%)	Fe 2p$_{1/2}$(%)
0.0	Co^{2+}	Co^{2+}	710.03(66.22%)	723.51(66.50%)
	Co^{3+}	Co^{3+}	711.85(33.78%)	725.53(33.50%)
0.2	779.70(71.09%)	794.66(72.34%)	709.90(68.96%)	723.41(70.01%)
	782.27(28.91%)	796.05(27.66%)	711.79(31.04%)	725.64(29.99%)
0.4	779.67(69.20%)	794.68(70.08%)	710.13(70.92%)	723.33(71.43%)
	780.69(30.80%)	796.15(29.02%)	712.46(29.08%)	724.80(28.57%)
0.6	779.59(65.92%)	794.59(66.32%)	710.28(69.93%)	723.34(70.45%)
	780.73(34.08%)	796.15(29.02%)	713.41(30.06%)	724.64(29.55%)
0.8	779.24(66.66%)	794.49(66.67%)	709.66(62.32%)	722.83(59.45%)
	780.25(33.34%)	796.16(33.33%)	711.72(37.68%)	724.09(40.55%)
1	779.54(72.42%)	794.75(70.34%)	Fe^{2+}	Fe^{2+}
	780.51(27.58%)	796.37(29.66%)	Fe^{3+}	Fe^{3+}

Table 4   XPS binding energies relative to the perovskites $LaCo_xFe_{1-x}O_3$

O 1s (eV)	0.0 (%)	0.2 (%)	0.4 (%)	0.6 (%)	0.8 (%)	1.0 (%)
Lattice oxygen	54.34	52.95	51.49	46.49	46.17	45.97
Surface oxygen	38.17	40.28	41.53	47.84	46.58	45.34
Absorbed oxygen	7.49	6.77	6.98	5.67	7.25	8.69
Surface/lattice	0.70	0.76	0.81	1.03	1.01	0.99

$$(\alpha h\nu)^m = K(h\nu - E_g)$$

where α is the optical absorption coefficient, $h\nu$ is the photon energy, and K is a constant. The value of m depends on the nature of the transition in a semiconductor. Using theoretical calculations, the value of m was found to be 2 for this case, which describes a direct transition type model. The band gap energy of the semiconductor can be obtained by plotting $(\alpha h\nu)^2$ against the photon energy $h\nu$ and extrapolating the plot line as represented in Fig. 6b.

Table 5 shows the band gap energies determined for the $LaCo_xFe_{1-x}O_3$ materials ($x = 0, 0.2, 0.4, 0.6, 0.8, 1$), which were found to be 2.07, 1.78, 1.70, 1.68, 1.80 and 1.84 eV, respectively.

The lowest calculated band gap energy of 1.68 eV was obtained for $x = 0.6$. The highest energy band gap of 2.07 eV was calculated for the sample with no Co-doping. These data demonstrate the potential to control the optical response of $LaFeO_3$ perovskites by controlling the band gap,[49] and support the findings of subsequent photocatalytic performance tests. Even that Fe and Co both belongs to the typical transition metals, Fe^{3+} and Co^{3+} are different in either E_g electron number or the feasibility of reduction to 2+ valance state. So it is rational to expect that the mixing ration between Fe and Co should influence the band structure of $LaCo_xFe_{1-x}O_3$.

The correlation between the electronic band gap energy of a material and its photocatalytic activity is well understood. Narrower band gap facilitates more visible light absorption and so might increase the photocatalysis performance. In addition to determining band gap it is also important to study the conduction band (CB) and valence band (VB), and absolute

Table 5   Band gap of each $LaCo_xFe_{1-x}O_3$ nanoparticle in different Co rate (form Co = 0 to 1.0)

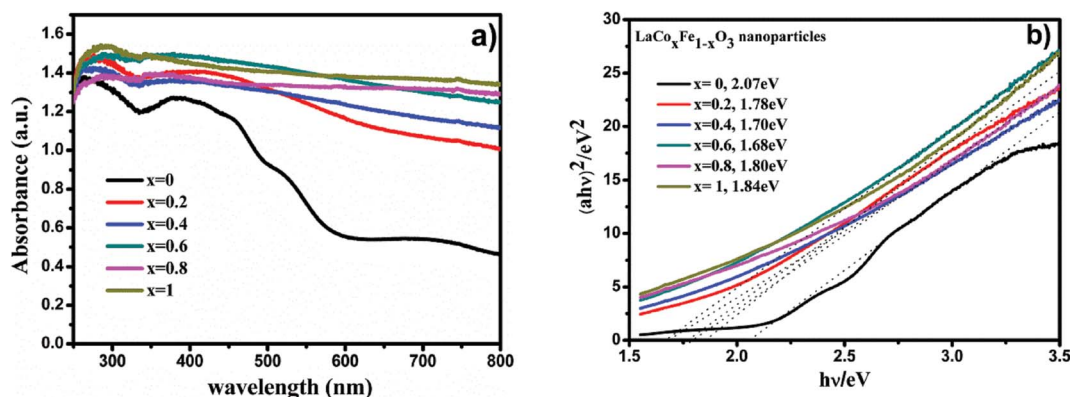| Co/Fe	0.0	0.2	0.4	0.6	0.8	1.0
E_g (eV)	2.07	1.78	1.70	1.68	1.80	1.84

Fig. 6 UV-Vis diffuse reflectance spectra of $LaCo_xFe_{1-x}O_3$ nanoparticle in different Co rate (a), plots of $(\alpha h\nu)^2$ versus photon energy of $LaCo_xFe_{1-x}O_3$ sample (b).

energies in relation to the reduction and oxidation potentials. The potential of the CB edges (E_{CB}) can be measured using the Mott–Schottky (MS) relationship. As can be seen in Fig. 7a–f, the typical n-type semiconductor characteristics of all samples were revealed by observing the positive slopes of the MS plots. The E_{CB} of the samples was determined against a Ag/AgCl reference electrode in aqueous solution. The E_{CB} of LaCo$_x$Fe$_{1-x}$O$_3$ nanoparticles with x values ranging from 0 to 1 were −0.314, −0.289, −0.263, −0.258, −0.276 and −0.305 V, respectively. The VB potential (E_{VB}) values for the samples can be estimated approximately using the following equation: $E_{VB} = \chi - E_e + 2E_g$, $E_{CB} = E_{VB} - E_g$, where χ is the electronegativity of the atom, E_{CB} is the CB edge potential, E_e is the energy on the hydrogen scale (4.5 eV) and E_g is the optical band gap of the semiconductor.

Using the above results in combination with the band gap energies obtained from the diffuse reflectance spectra, the obtained values of E_{VB} were 1.756, 1.491, 1.437, 1.422, 1.524, and 1.535 V, respectively. The E_{VB} value for the sample with a Co-doping of 0.6 was found to be the lowest in the series (1.422 V). Photocatalytic performance of a material requires that the valence band electrons are excited to the conduction band into high-energy transition states, resulting in the formation of electron–hole pairs. A less positive VB position makes this excitation easier and enhances the redox potential of catalysts in photocatalytic processes. By considering the following half-equations:
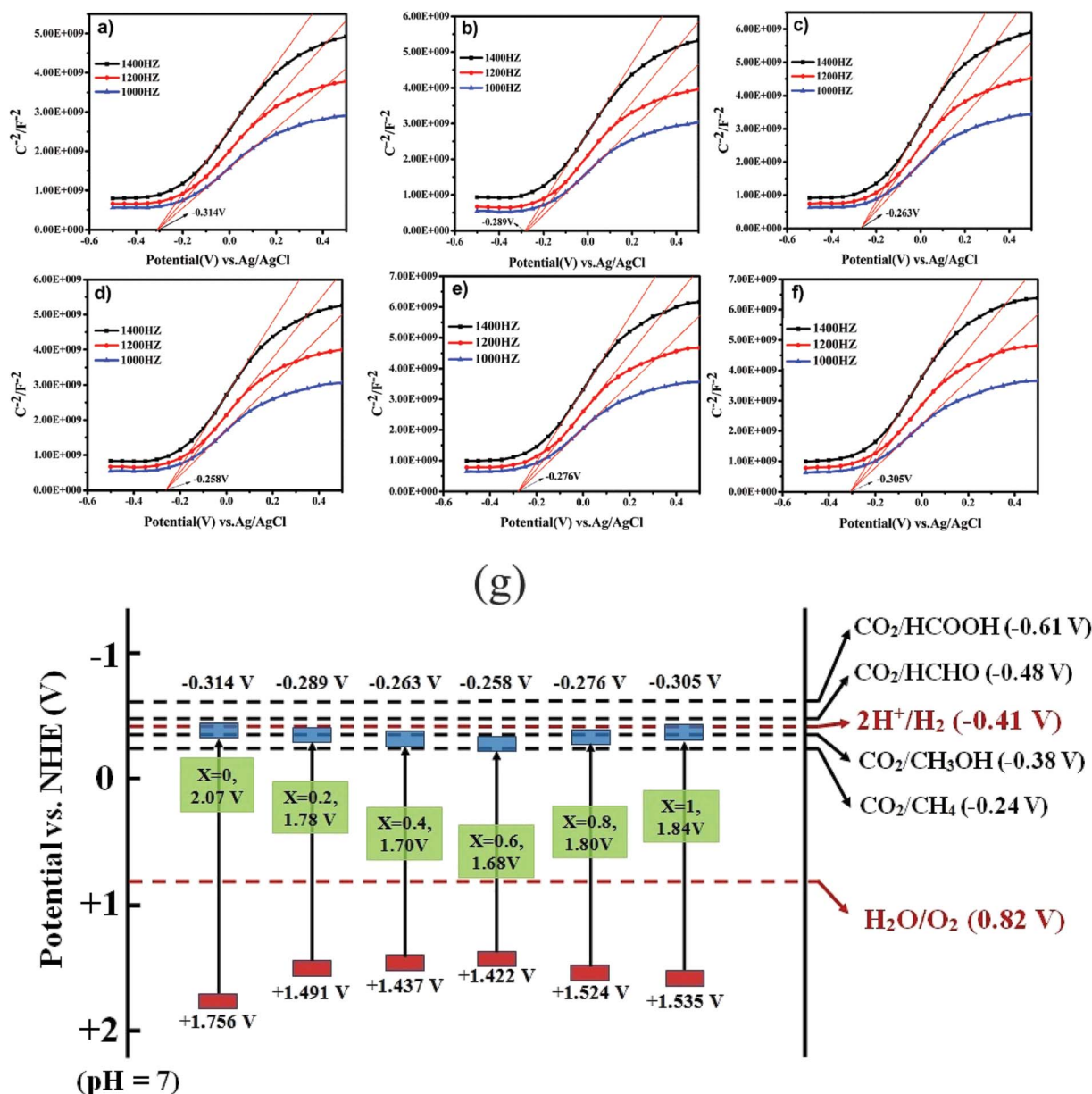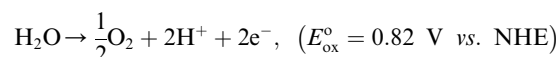
$$H_2O \rightarrow \frac{1}{2}O_2 + 2H^+ + 2e^-, \quad (E_{ox}^o = 0.82 \text{ V } vs. \text{ NHE})$$

Fig. 7 Mott–Schottky plots of LaCo$_x$Fe$_{1-x}$O$_3$ nanoparticle in different Co rate from 0 to 1 (a–f). A schematic illustration of the band structure of LaCo$_x$Fe$_{1-x}$O$_3$ nanoparticle (g).

$$CO_2 + 8e^- + 8H^+ \rightarrow CH_4 + 2H_2O, \ (E^o_{red} = -0.24 \ V \ vs. \ NHE)$$

It is possible to deduce that the VB values for all samples are more positive than $E^o(H_2O/H^+)$ and the CB values are more negative than $E^o(CO_2/CH_4)$. These results indicate that the reactions could be initiated with photogenerated carriers (electrons and holes) in the irradiated $LaCo_xFe_{1-x}O_3$ nanoparticles, leading to CH_4 production through the adsorption of CO_2 and H_2O. All samples are black in color indicating a potential for efficient visible light absorption and higher photothermal catalytic efficiency.[24] This is roughly consistent with the photothermal catalytic performance data reported in Fig. 8.

Fig. 8a and b show CH_4 and CH_3OH generation and photothermal catalytic activity at different Co-doping rates, evaluated under photothermal conditions, 350 °C and visible light irradiation for 6 h. Fig. 8a and b show a significant catalytic activity increase with Co-doping at the B-site, when compared with $LaFeO_3$ perovskite. At the end of the 6 h reaction time, the methane yield for samples with different Co/Fe molar ratios was in the order of 0.6 > 0.4 > 0.2 > 0.8 > 1 > 0, a similar sequence was also observed for methanol yield. It is also clear from the data for all samples that photothermal catalytic activity increased over time. The production of CH_4 and CH_3OH from CO_2 and H_2O, under photothermal conditions after 6 h for $x = 0, 0.2, 0.4, 0.6, 0.8$ and 1, were 138.59, 322.84, 355.46, 437.28, 193.90, 224.70 μmol g^{-1} and 3.45, 9.61, 13.01, 13.75, 5.28, 4.72 μmol g^{-1} respectively (see Table 6). Looking more closely at the best performing Co-doped material based on the data described ($x = 0.6$), it is clear that CH_4 and CH_3OH generation over $LaCo_{0.6}Fe_{0.4}O_3$ catalyst are 3.2 and 4.0 times of that of pure $LaFeO_3$. It is also worth noting that two end compounds, pure $LaFeO_3$ and $LaCoO_3$, possess the lowest yield of CH_4 and CH_3OH. These results demonstrate that partial substitution of Fe with Co at the B-site leads to better catalytic performance under photothermal conditions.

Energy conversion efficiency of photothermal reduction of CO_2 with H_2O vapor to CH_4 and CH_3OH over $LaCo_xFe_{1-x}O_3$ perovskites can be expressed more adequately by total yield

Table 6 Photothermal catalytic activity and physical properties of the $LaCo_xFe_{1-x}O_3$ perovskites

Sample (x)	The first hour production (μmol g^{-1})		Production after 6 h (μmol g^{-1})		Total yield (%)
Produce	CH_4	CH_3OH	CH_4	CH_3OH	$CH_4 + CH_3OH$
0.0	93.86	1.68	138.59	3.45	2.44732
0.2	192.80	5.43	322.84	9.61	5.72843
0.4	213.01	7.72	355.46	13.01	6.34893
0.6	275.83	9.61	437.28	13.75	7.77147
0.8	114.27	2.63	193.90	5.28	3.96264
1.0	126.03	2.42	224.70	4.72	3.42235

(conversion rate of CO_2 to CH_4 and CH_3OH) STM (solar-to-methane or methanol) efficiency (S2†). As shown in Table S2,† the best overall CO_2 conversion rate can reach 7.77% for $x = 0.6$ $LaCo_xFe_{1-x}O_3$. Considering the fact that it is not possible to avoid gas leakage in our reactor (only simple sealing implemented) at elevated temperature, it is rational to expect that a higher total yield can be expected if a high pressure reactor can be built in the future. The highest STM efficiency of CH_4 and CH_3OH for $x = 0.6$ $LaCo_xFe_{1-x}O_3$ can reach 0.6% and 0.019% respectively. Unfortunately, there is not much reported data can be used to compare the performance of our catalyst without noble metal loaded. F. Saladin[51] had reported an accumulated CH_4 yield of 24 μmol g^{-1} at 200 °C after 6 h UV light irradiation with CO_2 and H_2O as raw material and Degussa P25 TiO_2 as catalyst in a very similar photothermal catalysis study.

In conclusion, the catalytic activity determined for $LaCo_xFe_{1-x}O_3$ nanoparticles is consistent with the various characterization results. More specifically we can speculate that the influencing factors on catalytic activity may be correlated to surface area, crystallite size, band gap and oxygen vacancies based on the following observations. First the greater the surface area, the greater the area for photon radiation and catalytic reaction sites. Second, the small pores size can improve their catalytic performance by increasing the
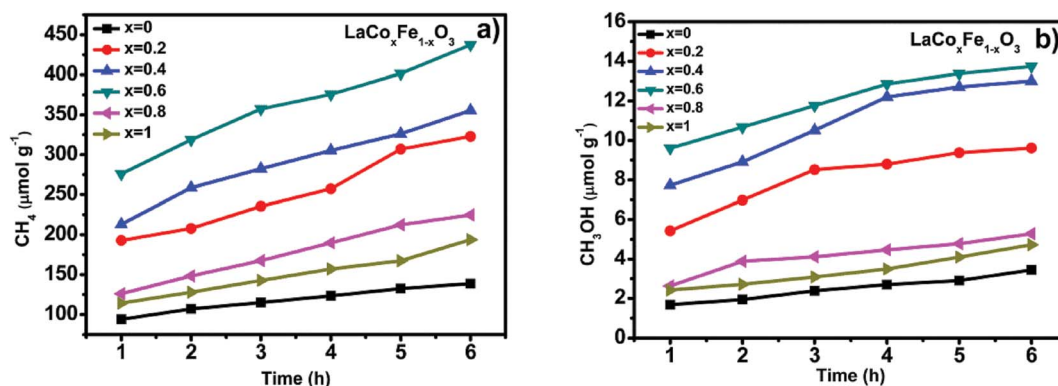

Fig. 8 CH_4 generation over the under visible light irradiation and heating condition at 350 °C (a) and CH_3OH generation over the under visible light irradiation and heating condition at 350 °C (b).
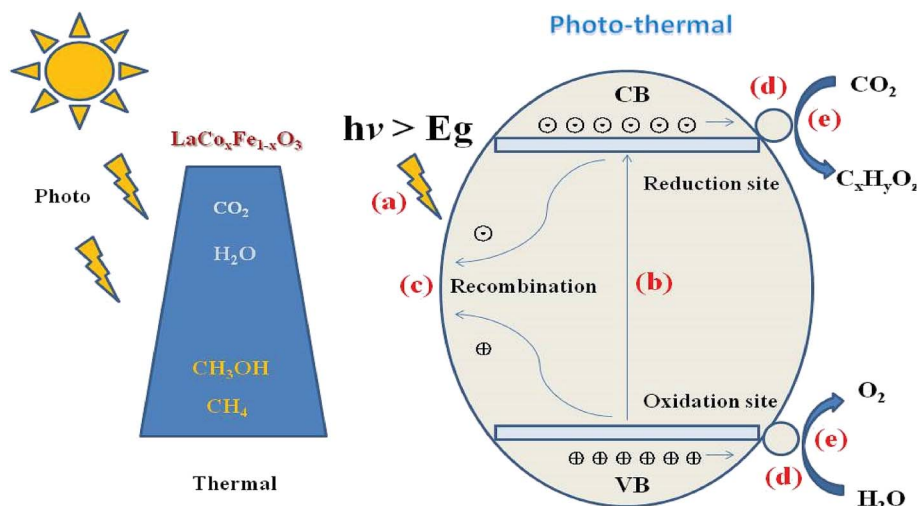
Fig. 9 Schematic diagram of the combined photo- and thermal-catalytic reduction of CO_2 with H_2O vapor to CH_4 in one system over $LaCo_xFe_{1-x}O_3$ perovskites.

adsorption efficiency of the reactants. However, the characterization results of the samples in these two aspects shows that there is no significant difference in our experiments. Furthermore, the smaller the crystallite size, the shorter the migration time of photoinduced charge carriers from the bulk to the surface, meaning that they have chance to reach to surface before recombination to improve the catalytic efficiency.[38] Lastly, we focus on the specific effects of band structure and oxygen vacancies on photothermal activity. By adjusting the band structure of the material, the band gaps of the Co-doped samples became smaller and the positions of the CB and VB became more suitable for CO_2 photo reduction. We reported that the minimum band gap is 1.68 eV when Co content is 0.6. This contributes to the effective separation process of electron–hole pairs and also helps to inhibit the recombination of photoinduced charge carriers. And oxygen vacancies can facilitate the separation of water and in the reaction process to improve the catalytic efficiency.[19] Additionally, our observations may depend on the photo-thermal coupling effect which could have resulted from our experimental conditions which used simultaneous irradiating with visible light and heating. The combination of all of these factors can be regarded as favorable for photocatalytic reaction give the observed increase in the photocatalytic activity.

The reaction mechanism for the photothermal reduction of CO_2 to CH_4 with H_2O vapor over catalyst samples is shown in Fig. 9. The catalytic process involves five steps (a)–(d): (a) the first is irradiation of the catalyst surface by a visible light source. This process requires a large catalyst surface area for exposure to radiation from the sun. Since $LaCo_xFe_{1-x}O_3$ perovskite surfaces can adsorb CO_2 and H_2O molecules, the catalyst surface is vital for developing its role in the photocatalytic reduction of CO_2. (b) An electron of the valence band absorbs energy from a photon greater than or equal to the band gap energy, and transitions to a high energy state in the conduction band, resulting in the formation of an electron–hole pair

(carrier). Considering Fig. 7g and the reported data, we can conclude that the VB edge position of all $LaCo_xFe_{1-x}O_3$ compounds is more negative than that needed for the production of CH_4. It is therefore believed that methane can be mainly produced through photocatalytic reduction of CO_2. However, the VB edge of all $LaCo_xFe_{1-x}O_3$ compounds is not negative enough for the production of CH_3OH through photocatalytic reduction process. So we have to point out that the production of small amount of CH_3OH in our study might be the result of thermal catalysis, the reaction process can be referred to that described in ESI S3.† (c) Most of the carriers will recombine and the energy produced will disperse out in the form of thermal energy or photons. (d) At the same time, the carriers produced by electronic excitation migrate to the surface of the sample or reach the interface with further aid. Furthermore, the corresponding active sites of oxidation and reduction are formed. Finally, the carriers which have been photogenerated and transmitted to the surface of the catalyst react with CO_2 and H_2O molecules to obtain O_2 and H^+ and various hydrocarbons.[50] In addition, methane, methanol and other hydrocarbons can be generated by interacting CO_2 with H^+ and electrons, which according to the reduction of force can accept different numbers of electrons. In summary, the photothermal catalytic activity of $LaFeO_3$ was enhanced by Co-doping, which adjusted the band structure and reduced the band gap. These findings may be of importance for a variety of applications.

Conclusions

We successfully synthesized $LaCo_xFe_{1-x}O_3$ ($x = 0$, 0.2, 0.4, 0.6, 0.8, 1) nanoparticles using the sol–gel process by Co-doping to achieve different molar ratios at the B-site of the ABO_3 style perovskite model. Their structure, phase components, morphology, surface area, and electronic structure were investigated using XRD, SEM, TEM, BET and UV-vis characterization methods, and their catalytic properties were investigated. Under

photothermal reaction conditions, the Co-doped catalysts displayed better catalytic performance for the reduction of CO_2 to CH_4 (with H_2O) than $LaFeO_3$. It is well known that the electronic structure of a material can be influenced by doping with transition metal elements. In this study Co incorporation resulted in significant changes to the valence and conduction band positions, which reduced the band gap. The CH_4 and CH_3OH generation rates for the reduction of CO_2 to CH_4 (with H_2O) using $LaCo_{0.6}Fe_{0.4}O_3$ as the catalyst, were enhanced 3.2 and 4.0 times respectively compared with $LaFeO_3$ under the same photothermal reaction conditions. This confirms that the partial substitution of Fe by Co at the B-site of $LaFeO_3$ perovskite manifests in greater catalytic activity. Based on these findings, we believe that the high catalytic activity is associated with small crystallite size, large specific surface area, small porous size, small band gap and suitable valence and conduction band positions of the material. However, the most important is to adjust the valence band to the conduction better position to achieve optimization of the material band structure, all of which would improve the CO_2 and H_2O adsorption and reaction at the catalyst surface. These results may further promote the application of $LaCo_xFe_{1-x}O_3$ in catalysis, environmental cleaning and solar fuel production.

Conflicts of interest

There are no conflicts to declare.

Notes and references

1 C. C. Lo, C. H. Hung, C. S. Yuan and J. F. Wu, *Sol. Energy Mater. Sol. Cells*, 2007, **91**, 1765–1774.

2 P. Goodwin, R. G. Williams and A. Ridgwell, *Nature*, 2015, **8**, 29–34.

3 T. L. Frolicher and D. J. Paynter, *Environ. Res.*, 2015, **10**(7), 075002.

4 J. Gibbins and H. Chalmers, *Energy Policy*, 2008, **36**, 4317–4322.

5 J. C. M. Pires, F. G. Martins, M. C. M. Alvim-Ferraz and M. Simões, *Chem. Eng. Res. Des.*, 2011, **89**, 1446–1460.

6 E. R. Bobicki, Q. X. Liu, Z. H. Xu and H. B. Zeng, *Prog. Energy Combust. Sci.*, 2012, **38**, 302–320.

7 G. Centi, E. A. Quadrelli and S. Perathoner, *Energy Environ. Sci.*, 2013, **6**, 1711–1731.

8 J. Low, B. Cheng, J. Yu and M. Jaroniec, *Adv. Energy Mater.*, 2016, **3**, 24–35.

9 L. Yuan and Y. J. Xu, *Appl. Surf. Sci.*, 2015, **342**, 154–167.

10 Y. Fu, D. Sun, Y. Chen, R. Huang, Z. Ding, X. Fu and Z. Li, *Angew. Chem.*, 2012, **124**, 3364–3367.

11 M. R. Hoffmann, W. Y. Choi and D. W. Bahnemann, *Chem. Rev.*, 1995, **95**, 69–96.

12 F. Achouri, S. Corbel, L. Balan, K. Mozet, E. Girot and G. Medjahdi, *Mater. Des.*, 2016, **101**, 309–316. l reviews, 1995, 95(1), 69–96.

13 A. A. Ismail and D. W. Bahnemann, *J. Phys. Chem. C*, 2009, **113**, 7429–7435.

14 K. Sayama, *Nanostructured Photocatalysts*, Springer International Publishing, 2016, pp. 429–442.

15 A. Fujishima and K. Honda, *Nature*, 1972, **238**, 37–38.

16 E. V. Kondratenko, G. Mul, J. Baltrusaitis, G. O. Larrazábal and J. Pérezramírez, *Energy Environ. Sci.*, 2013, **6**, 3112–3135.

17 Y. F. Xu, M. Z. Yang, B. X. Chen, X. D. Wang, H. Y. Chen, D. B. Kuang and C. Y. Su, *J. Am. Chem. Soc.*, 2017, **139**, 5660–5663.

18 H. Yoneyama, Y. Yamashita and H. Tamura, *Nature*, 1979, **282**(5741), 817–818.

19 L. Wang, Y. Wang, Y. Cheng, Z. Liu, Q. Guo, M. N. Ha and Z. Zhao, *J. Mater. Chem. A*, 2016, **4**, 5314–5322.

20 M. N. Ha, G. Lu, Z. Liu, L. Chao and Z. Zhao, *J. Mater. Chem. A*, 2016, **4**, 13155–13165.

21 H. Qin, J. Hu, J. Chen, H. Niu and L. Zhu, *J. Magn. Magn. Mater.*, 2003, **263**, 249–252.

22 A. A. Saad, W. Khan, P. Dhiman, A. H. Naqvi and M. Singh, *Electron. Mater. Lett.*, 2013, **9**, 77–81.

23 L. Chvez-Guerrero, B. Medina-Lott, R. F. Cienfuegos, M. A. Garza-Navarro, R. N. Vannier and A. Ringue, *J. Rare Earths*, 2015, **33**, 277–281.

24 P. Datta, P. Majewski and F. Aldinger, *Mater. Chem. Phys.*, 2007, **102**, 240–244.

25 Z. Wang, C. Chen, C. Feng, J. Wang, B. Zou and M. Zhao, *Acta Phys.-Chim. Sin.*, 2008, **24**, 375–378.

26 C. Feng, S. Ruan and J. Li, *Sens. Actuators, B*, 2011, **155**, 232–238.

27 A. Benali, S. Azizi and M. Bejar, *Ceram. Int.*, 2014, **40**, 14367–14373.

28 R. Dridi, A. Mhamdi and A. Labidi, *Mater. Chem. Phys.*, 2016, **182**, 498–502.

29 A. Leontiou, A. Ladavos and P. Pomonis, *Appl. Catal., A*, 2003, **241**, 133–141.

30 R. De Lima, M. Batista and M. Wallau, *Appl. Catal., B*, 2009, **90**, 441–450.

31 Y. Wang, X. Cui and Y. Li, *Dalton Trans.*, 2013, **42**, 9448–9452.

32 M. Ha, F. Zhu and Z. Liu, *RSC Adv.*, 2016, **6**, 21111–21118.

33 L. Liu, Y. Cheng and Z. Liu, *RSC Adv.*, 2016, **6**, 83814–83819.

34 S. Tijare, M. Joshi and P. Padole, *Int. J. Hydrogen Energy*, 2012, **37**, 10451–10456.

35 G. Iervolino, V. Vaiano and D. Sannino, *Int. J. Hydrogen Energy*, 2016, **41**, 959–966.

36 L. Jing, Y. Qu and H. Su, *J. Phys. Chem. C*, 2011, **115**, 12375–12380.

37 H. Su, L. Jing and K. Shi, *J. Nanopart. Res.*, 2010, **12**, 967–974.

38 S. Farhadi, M. Amini and F. Mahmoudi, *RSC Adv.*, 2016, **6**, 102984–102996.

39 S. Li, L. Jing and W. Fu, *Mater. Res. Bull.*, 2007, **42**, 203–212.

40 H. Tanaka and M. Misono, *Curr. Opin. Solid State Mater. Sci.*, 2001, **5**, 381–387.

41 K. Parida, K. Reddy and S. Martha, *Int. J. Hydrogen Energy*, 2010, **35**, 12161–12168.

42 L. Liotta, F. Puleo and V. La Parola, *Electroanalysis*, 2015, **27**, 684–692.

43 T. Lin, G. Seshadri and J. Kelber, *Appl. Surf. Sci.*, 1997, **119**, 83–92.

44 E. García-López, G. Marcì and F. Puleo, *Appl. Catal., B*, 2015, **178**, 218–225.

45 B. Liu, Y. Zhang and L. Tang, *Int. J. Hydrogen Energy*, 2009, **34**, 435–439.

46 L. Liu, W. Fan and X. Zhao, *Langmuir*, 2012, **28**, 10415–10424.

47 F. Puleo, L. Liotta and P. La, *Phys. Chem.*, 2014, **16**, 22677–22686.

48 W. Kim, M. Choi and K. Yong, *Sens. Actuators, B*, 2015, **209**, 989–996.

49 J. Wang, P. Guo and M. Dou, *RSC Adv.*, 2014, **4**, 51008–51015.

50 S. Habisreutinger, L. Schmidt Mende and J. Stolarczyk, *Angew. Chem., Int. Ed.*, 2013, **52**, 7372–7408.

51 F. Saladin, *et al.*, *J. Chem. Soc., Faraday Trans.*, 1997, **93**, 4159–4163.